AFRL-AFOSR-VA-TR-2019-0224

High-Throughput Experimentally and Computationally Guided Discovery of Next Generation High-Temperature Shape Memory Alloys

Joost Vlassak
HARVARD COLLEGE PRESIDENT & FELLOWS OF

08/01/2019
Final Report

Air Force Research Laboratory
AF Office Of Scientific Research (AFOSR)/ RTB1
Arlington, Virginia 22203
Air Force Materiel Command

REPORT DOCUMENTATION PAGE

Form Approved
OMB No. 0704-0188

1. REPORT DATE *(DD-MM-YYYY)*	**2. REPORT TYPE**	**3. DATES COVERED** *(From - To)*
31-07-2019	Final Report	1 May 2016 to 30 April 2019

4. TITLE AND SUBTITLE
HIGH-THROUGHPUT EXPERIMETALLY AND COMPUTATIONALLY GUIDED DISCOVERY OF NEXT GENERATION HIGH-TEMPERATURE SHAPE MEMORY ALLOYS

5a. CONTRACT NUMBER

5b. GRANT NUMBER
FA9550-16-1-0180

5c. PROGRAM ELEMENT NUMBER

6. AUTHOR(S)
Vlassak, Joost, J.
Arróyave, Raymundo

5d. PROJECT NUMBER

5e. TASK NUMBER

5f. WORK UNIT NUMBER

7. PERFORMING ORGANIZATION NAME(S) AND ADDRESS(ES)
Harvard University, 29 Oxford St, Cambridge MA 02138
Texas A&M University, College Station, TX 77843

8. PERFORMING ORGANIZATION REPORT NUMBER
n/a

9. SPONSORING/MONITORING AGENCY NAME(S) AND ADDRESS(ES)
Air Force Office of Sponsored Research
c/o Dr Ali Sayir
875 North Randolph Street, Arlington, Virginia 22203

10. SPONSOR/MONITOR'S ACRONYM(S)
AFOSR

11. SPONSOR/MONITOR'S REPORT NUMBER(S)
n/a

12. DISTRIBUTION/AVAILABILITY STATEMENT
n/a

13. SUPPLEMENTARY NOTES

14. ABSTRACT
We have developed a framework for the discovery of novel high-temperature shape memory alloys by combining high-throughput experimental techniques, high-throughput computational methods, and statistical analysis/machine learning techniques. We have fabricated a novel resistance sensor array for the combinatorial screening of shape memory alloys, built a binary alloy database, and developed an efficient experiment design technique. An in-depth experimental-computational study on a broad range of Cu-Zr-X shape memory alloys shows that DFT simulations are a useful tool to guide the experimental development of shape memory alloys provided relevant energy terms are taken into account.

15. SUBJECT TERMS
High-temperature shape memory alloys, nanocalorimetry, Cu-Zr-X, DFT, efficient experiment design technique, resistance sensors

16. SECURITY CLASSIFICATION OF:			**17. LIMITATION OF ABSTRACT**	**18. NUMBER OF PAGES**	**19a. NAME OF RESPONSIBLE PERSON**
a. REPORT	**b. ABSTRACT**	**c. THIS PAGE**			Joost J. Vlassak
				27	**19b. TELEPHONE NUMBER** *(Include area code)* (617) 496 0424

AFOSR Final Performance Report

Project Title: **High-throughput experimentally and computationally guided discovery of next generation high-temperature shape memory alloys**

Award #: **FA9550-16-1-0180**

Period of Performance: 1 May 2018 to 30 April 2019

Program Manager: Dr. Ali Sayir
Director, High Temperature Aerospace Materials Program
AFOSR/NA
801 North Randolph Street, Room 732
Arlington, VA 22203-1977
Ali.Sayir@afosr.af.mil

Principle Investigator: Prof. Joost J. Vlassak
School of Engineering and Applied Sciences
Harvard University
Cambridge, MA 02138
(617) 496-0424
vlassak@esag.deas.harvard.edu

Prof. Raymundo Arróyave
Department of Materials Science and Engineering
Texas A&M University
College Station, TX 77843
raymundo.arroyave@tamu.edu

HIGH-THROUGHPUT EXPERIMENTALLY AND COMPUTATIONALLY GUIDED DISCOVERY OF NEXT GENERATION HIGH-TEMPERATURE SHAPE MEMORY ALLOYS

Joost J. Vlassak, Raymundo Arróyave

Abstract

The goal of this project is to develop a framework for the discovery of novel high-temperature shape memory alloys by combining high-throughput experimental techniques, high-throughput computational methods, and statistical analysis/machine learning techniques. This framework is implemented using the Cu-Zr SMA system as an exemplar. As part of this project, we have developed and fabricated a novel resistance sensor array for the combinatorial screening of shape memory alloys. These sensor arrays are inexpensive and provide excellent temperature uniformity, which is critical for detecting subtle changes in the phase composition of a material as a function of temperature. We have developed an efficient experiment design technique and built a binary alloy database. We have also carried out an in-depth experimental-computational study on a broad range of Cu-Zr-X (X = Co, Ni, Hf) shape memory alloys. The transformation behavior of these alloys, including crystallization, martensite-austenite transformation temperature, functional stability, and hysteresis, were investigated by nanocalorimetry. Ab initio simulations were used to determine the B2-Cm transformation pathway, evaluate the martensite and austenite lattice parameters, the relative phase stability, and the twin boundary energy as a function of composition. The phase stability as determined by ab initio simulations of the pristine martensite and austenite phases is not in agreement with experimental results. Adding energy terms representing the twin boundaries and the compatibility strain brings the simulations in close agreement with experimental observations. Based on these results, we suggest that DFT simulations are a useful tool to guide the experimental development of shape memory alloys, provided the relevant energy terms are taken into account.

Introduction

The overarching goal of this project is to accelerate the discovery of novel high-temperature shape memory alloys by combining high-throughput experimental techniques, high-throughput computational methods, and statistical analysis/machine learning techniques. The specific objectives include discovery of new regions in composition space that may contain novel HTSMAs by establishing a synergistic computational-experimental framework for materials discovery via identification of: i) the descriptors at the level of the electronic structure, crystal lattice and materials energy landscape that control the stability of the austenite phases against martensitic transformation, ii) systematic trends in the experimentally observed behavior of an HTSMA as a function of the compatibility between austenite and martensite, and iii) correlations by combining experiment and theory to pinpoint promising regions in the composition space likely to result in HTSMAs with large transformation temperatures, low hysteresis, high level of functional stability, and increased macroscopic mechanical compatibility between martensite variants. This framework is implemented using the Cu-Zr SMA system as an exemplar.

During the previous reporting period, experimental work focused on i) an investigation of the phase transformations in equiatomic CuZr thin-film samples by means of differential nano-calorimetry, ii) alloying the Cu-Zr system with Ni, and on iii) developing hotplate resistivity sensors for faster screening of materials. On the computational front, we sought to complement the experimental efforts by focusing on a deeper physical understanding of the energetics of the martensitic transformation in Cu-Zr and its alloys and to leverage this understanding to guide experiments.

In the current reporting period, we have designed and fabricated a new type of resistance sensor array for the combinatorial screening of materials. These sensors are inexpensive to fabricate and provide superior temperature uniformity, which is essential to detect subtle changes in the phase composition of a material. They can also be used if the phase transformation of interest has a very small enthalpic signature. We have built a binary alloy database and developed an efficient experiment design technique. We have carried out an in-depth experimental-computational study on a broad range of Cu-Zr-X (X = Co, Ni, Hf) shape memory alloys. Their transformation behavior, including crystallization, martensite-austenite transformation temperature, functional stability, and hysteresis, were investigated by nanocalorimetry. We have used *ab initio* simulations to determine the B2-Cm transformation pathway, evaluate the lattice parameters, the relative phase stability, and the twin boundary energy as a function of composition. We have shown that the phase stability as determined by ab initio simulations of the pristine martensite and austenite phases is not in agreement with experimental results. However, adding energy terms representing the twin boundaries and the compatibility strain brings the simulations in closer agreement with the experimental results. Based on these results, we suggest that DFT simulations are a useful tool to guide the experimental development of shape memory alloys, provided the appropriate energy terms are taken into account. Our study shows that Cu-Zr-Ni-based high temperature SMAs are

promising and merit further exploration. As a result of this study, thirteen papers have been published or submitted to archival journals, with several more in preparation. The following sections provide a detailed account of these activities.

1. Nanocalorimetry and *ab initio* study of ternary elements in Cu-Zr-based alloys

1.1 Experimental Technique

In this project, we use arrays of custom-made micromachined calorimetry sensors that were developed with prior AFOSR funding to study thin-film samples of Cu-Zr-X. Each sensor consists of a thin W layer that is patterned to serve both as heating element and resistance thermometer in a four-point measurement scheme. This heating element/thermometer is encapsulated in a thin SiN_x membrane that supports the heating element and insulates it from its surroundings. The samples of interest are deposited by magnetron co-sputtering in a high-vacuum system (base pressure is better than 10^{-4} Pa; 400 nm sample thickness). A shadow mask limits the area of deposition to the sample area of the sensor. By tailoring the power to the individual magnetrons in the system, samples of different composition can be deposited, either one at a time or as part of a composition spread. In a typical calorimetry scan, an electric current is supplied through the heating element, which causes Joule heating of sample and addendum. The measured current and voltage are then used to determine the power to the sensor and the resistance of the heating element, which is calibrated to temperature. To perform the measurements, the sensor array is placed in a probe card that is located inside a vacuum chamber with a base pressure of approximately 10^{-4} Pa. The data are acquired using a custom-built system described in [1].

1.2 Cu-Zr-X Phase Evolution

Figure 1a shows a typical first nanocalorimetry scan on an as-deposited $Cu_{50}Zr_{50}$ thin-film sample; Figure 1b depicts similar scans for as-deposited samples of several ternary Cu-Zr-X alloys. It is evident from the figures that all Cu-Zr-X samples go through the same series of reactions in the first scan – all scans have a strong exothermic peak followed by a smaller endothermic peak at more elevated temperature. The large peak in the calorimetry trace corresponds to the crystallization of the samples. Based on characterization and binary phase diagrams [2–5], it is likely that the crystallization product is two-phased and the small endothermic peak after the crystallization peak is a eutectoid reaction that forms the austenitic phase.

None of the samples show a martensitic transformation if they are cooled down immediately after the formation of the austenitic phase. In the case of the $Cu_{50-x}Zr_{50}Ni_x$ samples, a heat treatment of 20 seconds at 1100 K is needed before the martensitic transformation is observed. In the case of $Cu_{50-x}Zr_{50}Co_x$, and $Cu_{50}Zr_{50-x}Hf_x$, the samples need to be partially melted and re-solidified to show the martensitic transformation. This is the same heat treatment required for CuZr in our previous work [1]. We suggest that the B2 phase that forms during the eutectoid reaction has sufficient defects to prevent transformation to martensite on cooling. Possible causes are: (1) the austenitic phase is not fully stoichiometric as the B2 phase forms by reaction of Zr- and Cu-rich phases and

the composition may not be completely uniform; (2) insufficient ordering of the B2 phase. Either possibility indicates that the solid-state reaction needs a sufficiently long time to complete without giving a measurable calorimetric signal. This observation is not entirely surprising given that binary CuZr is a very good glass former and is expected to have sluggish kinetics [2,6]. The crystallization temperature of Cu-Zr-X gives an indication of the glass forming ability of the Ni, Co, and Hf-containing ternaries. Of the three alloys, Cu-Zr-Ni has the lowest crystallization temperature, i.e., the fastest kinetics, and presumably the poorest glass forming ability. A very brief (~ seconds) heat treatment at 1100K is sufficient to create an austenite that transforms to martensite at low temperature. The same heat treatment does not work for Cu-Zr-Hf or Cu-Zr-Co. These alloys need to be partially melted to re-grow defect-free crystals. Full melting of these alloys results in partially amorphous samples under the conditions of our experiments.

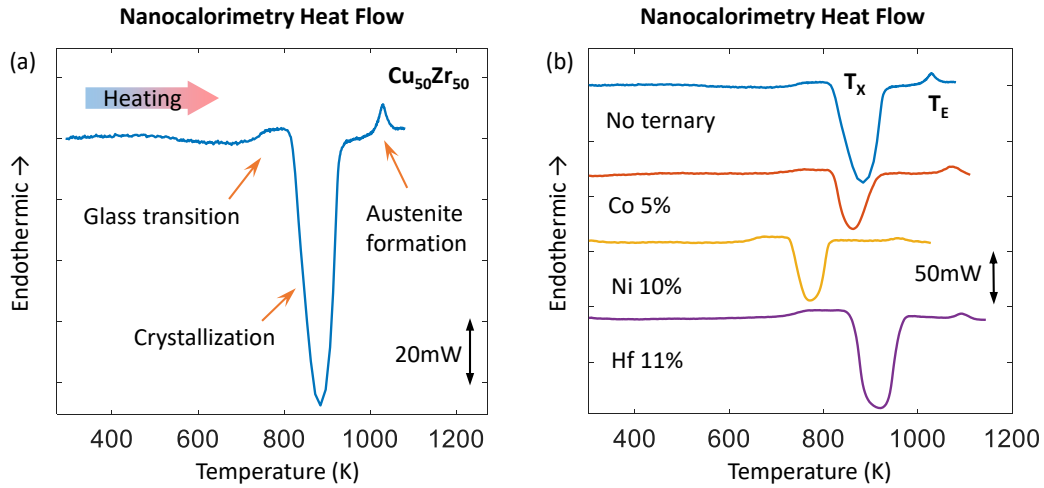

Figure 1. (a) First calorimetry scan on an as-deposited $Cu_{50}Zr_{50}$ sample and (b) first scans on as-deposited samples of several different CuZr-based alloys.

1.3 Transformation Temperatures and Hysteresis

Figure 2a shows a graph of the M-A transformation temperature as a function of composition. It is evident from the figure that replacing Cu with Ni or Zr with Hf increases the transformation temperature, although the effect of Hf is weaker than that of Ni. Replacing Cu with Co, on the other hand, slightly lowers the transformation temperature. The sample with 8% Co did not show a transformation even after being cooled to 150 K.

Figure 2b shows the hysteresis as determined by the temperature difference between the transformations on heating and cooling. All A-M transformations on cooling are typical athermal transformations. The addition of Ni and Co decreases the hysteresis, while Hf increases it, although the effects are small. The hysteresis observed for bulk CuZr alloys in previous studies ranges from

115 K to 250 K and depends on both heat treatment and the number of thermal cycles performed [8–11]. The hysteresis measured in this study is at the upper limit of this range, possibly due to small grain size of the samples [12].

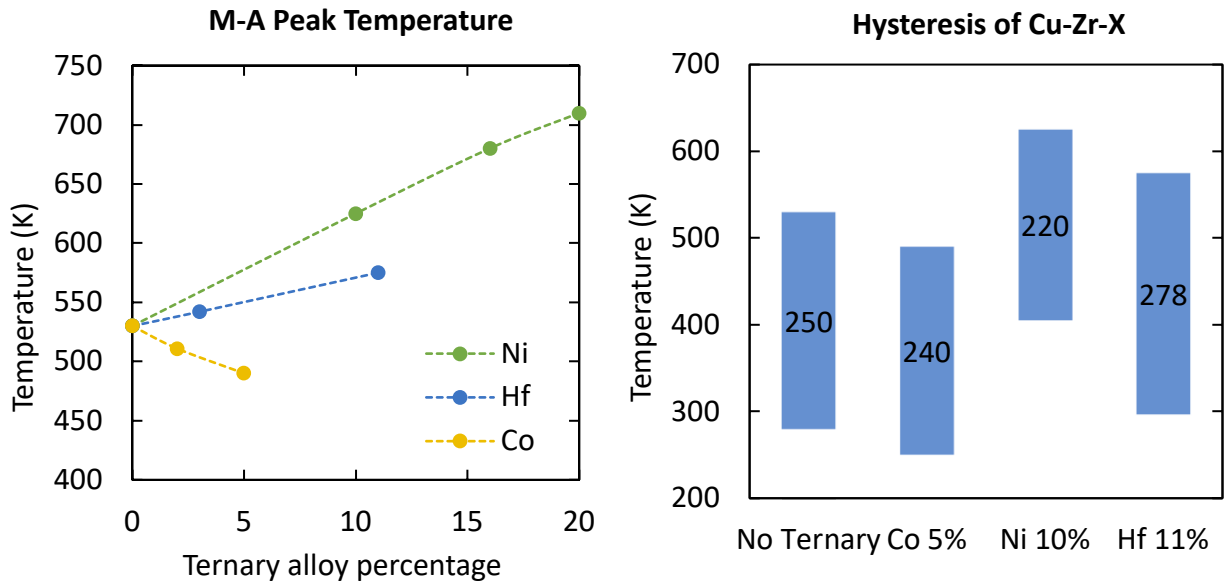

Figure 2. (a) List of martensite-austenite transformation peak temperatures (±5K error). (b) Hysteresis of M-A and A-M transformation peaks. Top of a bar is M-A peak temperature and bottom of a bar is A-M peak temperature. The numbers are the measured hysteresis (±10 K error).

1.4 Microstructure

Figure 3 shows TEM images of cross-sectional samples with compositions $Zr_{50}Cu_{34}Ni_{16}$ and $Cu_{50}Zr_{39}Hf_{11}$. Both images show clearly-defined martensitic twins, with widths ranging from 30 to 60 nm. The Ni-containing sample has a slightly larger width compared with the Hf-containing alloy. Previous studies showed that monoclinic Cm is the main martensitic phase in binary CuZr [8,13]. In this work, multiple diffraction images confirmed the existence of Cm structure. Another monoclinic structure, B19' (P21m space group), has also been reported [13], but was not identified by us. Since Cm is a superstructure of B19' [14], B19' has fewer diffraction spots and its diffraction pattern overlaps with that of Cm. The evidence thus suggests that there were no regions in the sample under investigation that consisted exclusively of B19'. Given the Cm structure, (021) and (001) twin planes were identified. As shown in Figure 6b, the martensite twins consist of much finer twins. This is in line with the general theory that martensite grows finely twinned structures that minimize the compatibility strain with the austenite and that result in leaf-like structures with a midrib [15,16].

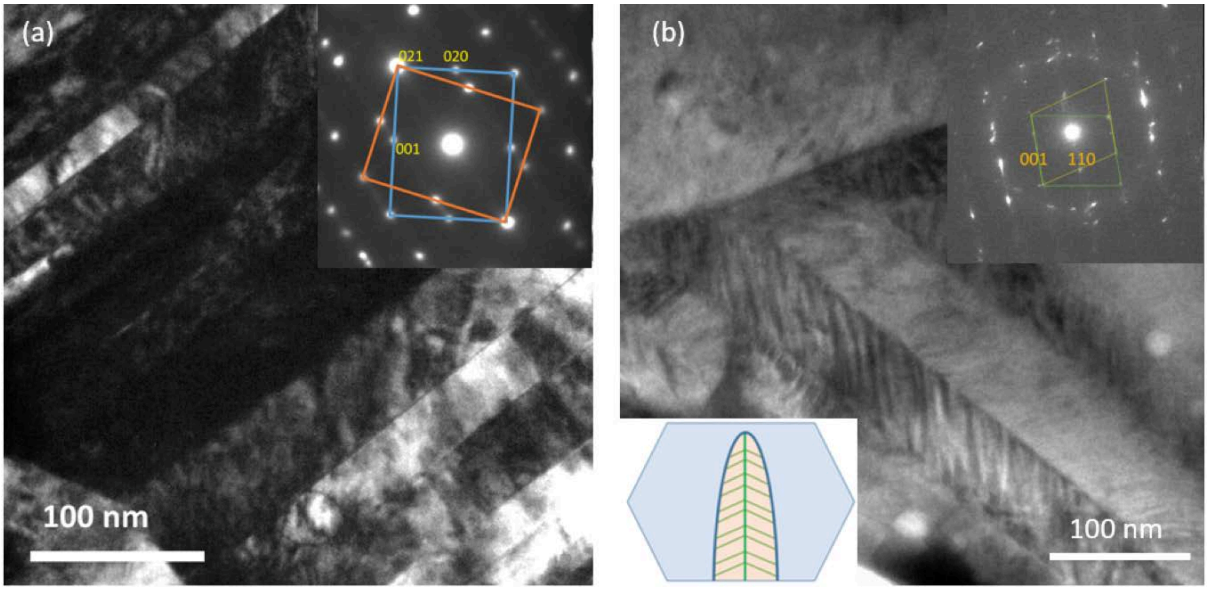

Figure 3. TEM images and corresponding diffraction patterns of (a) $Zr_{50}Cu_{34}Ni_{16}$ and (b) $Cu_{50}Zr_{39}Hf_{11}$. Inset in (b) shows possible microstructure of martensite growing in austenite.

1.5 Austenite-Martensite Lattice Compatibility

We used *ab initio* simulations to model the B2 and Cm phases of Cu-Zr-X with various concentrations of element X. The lattice parameters of the fully relaxed Cu-Zr-X B2 and Cm structures were used to calculate the transformation matrix, which maps the austenite lattice vectors onto the martensite lattice vectors. James et al. have shown that the middle eigenvalue of the transformation matrix is an measure for the compatibility between the austenite and the martensite phases [17,18]. The further the middle eigenvalue diverges from unity, the larger the mismatch on the martensite-austenite habit plane. Following the approach in [19], we computed the transformation matrices and their eigenvalues for the various Cu-Zr-X alloys. The middle eigenvalues are plotted in Figure 4. It is evident from the figure that Ni and Co bring λ_2 closer to 1, while Hf does not significantly change λ_2. Based on this result, one would expect the addition of Ni or Co to reduce the strain at the austenite martensite interface and thus reduce the transformation hysteresis as indeed observed experimentally (Figure 2b); the addition of Hf, on the other hand, should leave the hysteresis more or less unchanged, which is not observed. Of course, other factors may also affect hysteresis, e.g., the addition of ternary elements may introduce defects and make dislocation motion more difficult, which would tend to increase hysteresis.

1.6 Transformation Pathway and Energy Landscape

Thus far, the transformation pathway of B2-Cm has not been studied. Using the lattice correspondence, we modelled the B2-Cm energy landscape using four independent parameters, which are atomic shuffle in two directions, an orthorhombic distortion and a monoclinic distortion. A four-dimensional minimum energy pathway was extracted and further refined by the solid-state

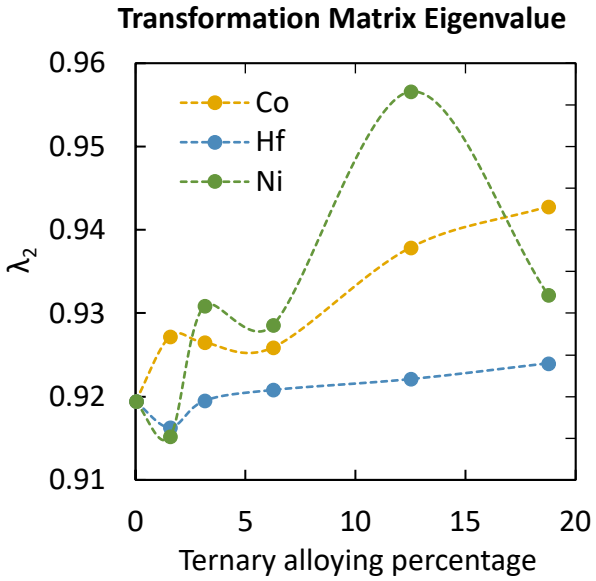

Figure 4. The second eigenvalue of the austenite-martensite transformation matrix. The second eigenvalue is an indicator of the compatibility between two phases. A unit value signifies no lattice mismatch. The lines connecting the data points are Bezier spline interpolations that serve as guides to the eye and have no physical meaning.

nudged elastic band method (SSNEB). We find that the B2-Cm transformation goes through Cmm2 as an intermediate structure (Figure 5). The B2-Cmm2 step takes place without an energy barrier, while the Cmm2-Cm step has a small energy barrier that is slightly higher than the energy of the initial B2 phase. The low energy barrier associated with the transformation could explain the preference for the B2-Cm transformation in CuZr.

The energy differences between austenite and martensite at 0 K are depicted as a function of composition in Figure 6. A negative value signifies that the martensite phase is more stable than the austenite. The calculations show that alloying CuZr with either Ni or Co should stabilize the martensite compared to the austenite, suggesting a higher martensite transformation temperature. Alloying with Hf does not have a significant effect on the energy difference between the two phases. These conclusions presuppose that there is no third phase that is more stable than either austenite or martensite when the alloying elements are added.

When comparing the experimental results (Figure 2a) with the M-A energy gap in Figure 6, it is clear that the computations and experiments are in agreement for Ni. In the case of Co, however, the computations suggest that Co should increase the transformation temperature up to a concentration of 6%, but the experiments show the opposite behavior. To rule out finite-temperature effects, calculations for these phases were also performed at finite temperatures, (Figure 7). These simulations took into account quasi-harmonic, electronic, and weak anharmonic contributions. With these terms added, we still see the energy difference crosses over zero at higher temperature for both the Ni and Co ternaries.

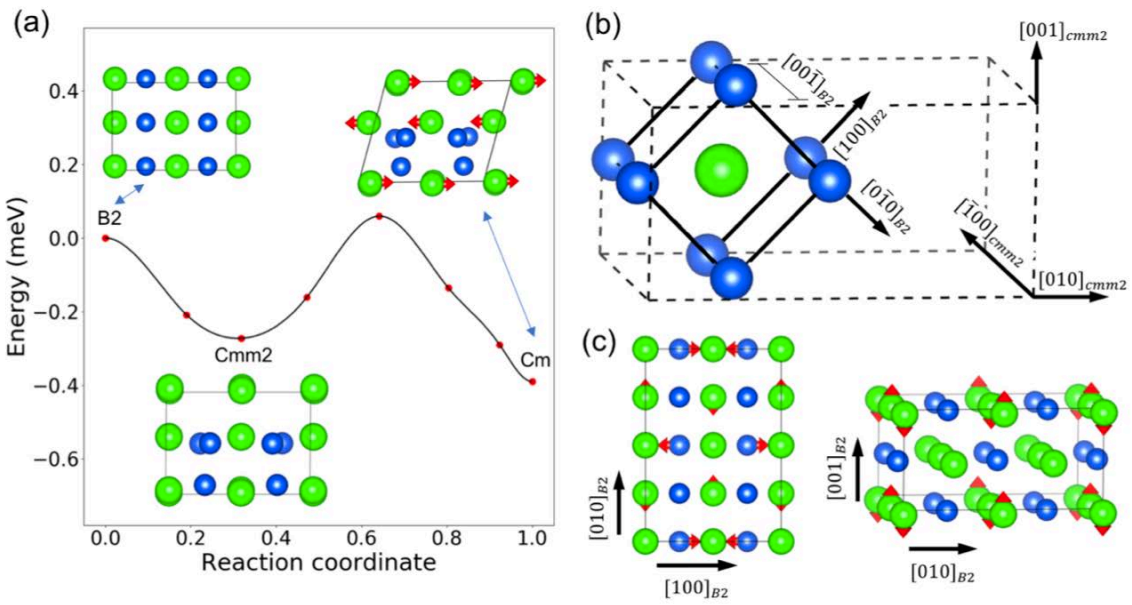

Figure 5. (a) Transformation pathway from B2 to Cm. Cmm2 is proposed as an intermediate structure. (b) Shows the lattice correspondence between B2 and Cmm2 and (c), the atomic shuffles along (001) and (100) planes, respectively, that constitute the Cmm2 structure. The transformation from B2 to Cmm2 is barrier-less, while the transformation from Cmm2 to Cm has a saddle point that is not much higher in energy than the B2 phase.

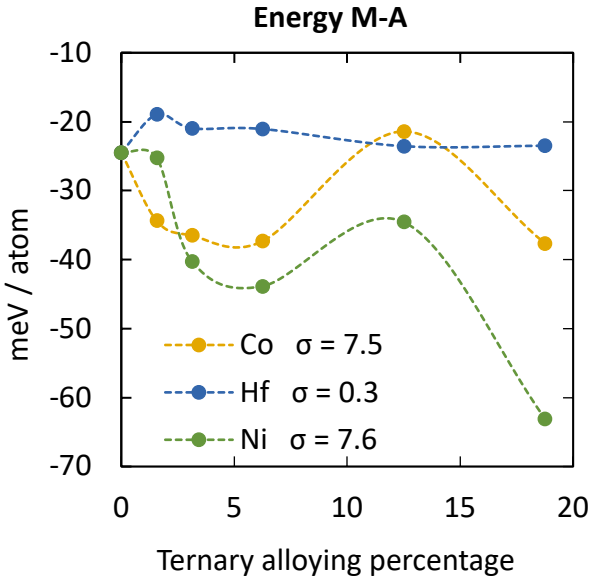

Figure 6. Energy difference between martensite and austenite. For each composition, more than one simulations with different atomic site replacements are performed. σ is the standard deviation in meV of these simulations. The lines connecting the data points are Bezier spline interpolations that serve as guides to the eye and have no physical meaning.

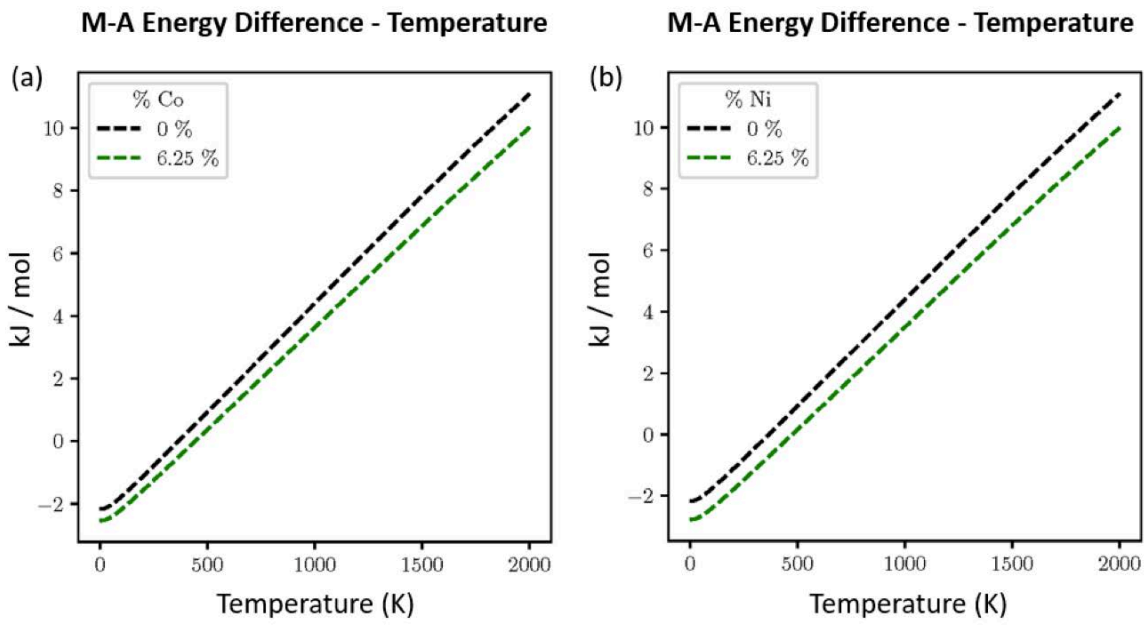

Figure 7. Finite temperature simulations. Each line shows the energy difference between martensite and austenite of a specific composition. At any given temperature, the M-A energy difference for Ni or Co ternary is larger than pure CuZr.

1.7 Twin Boundary Energy

It is evident from the results above that the energy difference between pristine martensite and austenite alone cannot explain the observed experimental trends. Energy terms beyond the energies of the pure phases need to be considered. For the martensitic transformation to proceed, martensite crystals need to grow in austenite creating austenite/martensite interfaces that can have very large compatibility strains depending on the value of λ_2. These compatibility strains are accommodated by twinning in the martensite and thus have a significant impact on the resulting microstructure. TEM imaging shows that Cu-Zr-X martensite indeed has a finely twinned microstructure (Figure 3b). This observation leads us to consider the contribution of the twin boundary energy to the total energy of the martensitic phase. We built a supercell that contains (021) twin planes and preformed relaxation using DFT. The energy of the (021) twin boundary was found by subtracting the energy of the untwinned structure from the twinned structure. The result is shown in Figure 8a. It is evident from the figure that both ternary alloys have a higher twin boundary energy than binary CuZr and that the twin boundary energy of Cu-Zr-Co is consistently higher than that of Cu-Zr-Ni. Very recent computational work by Sandoval shows that the twin boundary energy of a (001) twin in NiTi B19' is approximately 0.2 J/m^2 [20]. Compared to NiTi, the twin boundary energy of Cu-Zr-X is somewhat larger, but of the same order of magnitude.

To evaluate the impact of the twin boundary energy on the energy difference between the martensite and austenite, the twin boundary energy is converted to meV/atom for a twin spacing

of 3.7 nm, which is the average value measured for the Cu-Zr-X alloys using TEM. The energy difference between martensite and austenite (Figure 6) is fitted with a straight line to reduce error, although other forms of interpolation lead to similar conclusions. The results are shown in Figure 8b. The twin boundary energy has a significant impact on the energy gap between the two phases and this impact is different for different alloying elements: The energy gap increases with Ni content, as before, but remains nearly unchanged with the addition of Co. While there may be some uncertainty in the precise values of the twin boundary energies, it is clear from this example that the martensite twin spacing is small enough for the associated energy terms to alter the energy balance between the two phases. A simple comparison of the energies of the pristine phases is not sufficient to make predictions about the effect of alloying elements on the stability of the martensitic phase.

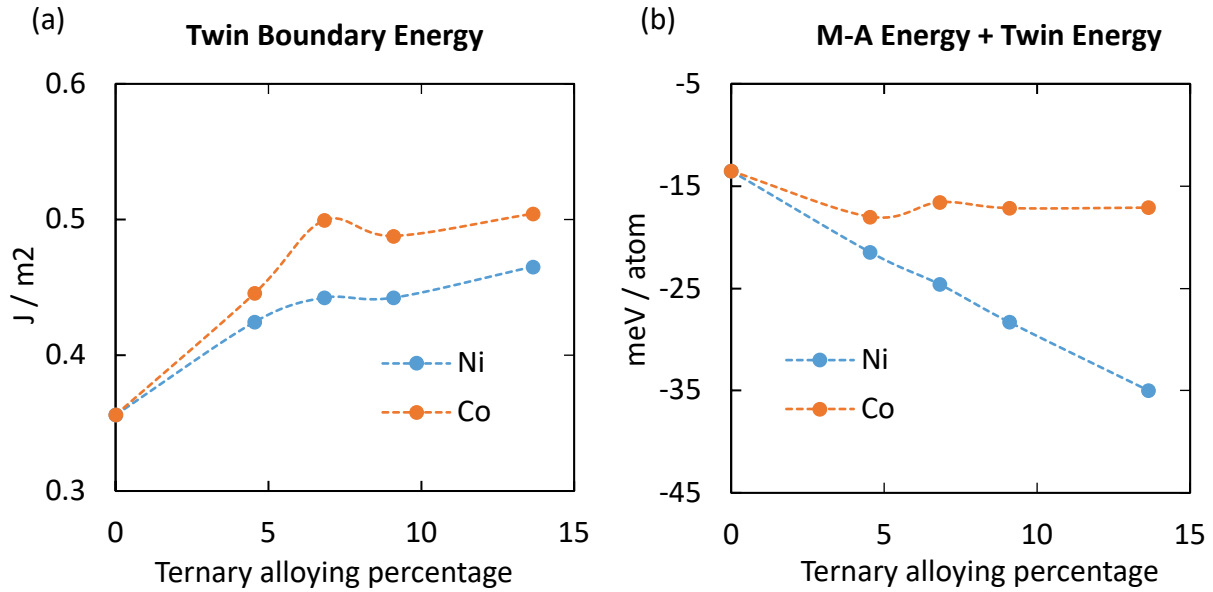

Figure 8. (a) Twin boundary energy as a function of composition; (b) Total energy difference between the martensite and austenite phases taking into account the presence of the twin boundaries. To reduce errors, the M-A energy is calculated using a linear fit to the energy difference between pristine martensite and austenite in Figure 9.

1.8 Balance of Twin Boundary Energy and M-A Strain Energy

The existence of twin boundaries adds to the total energy of the martensitic phase, making it less favorable relative to the parent austenitic phase. The twin boundaries are necessary to accommodate the compatibility strain associated with the martensitic transformations. In Figure 8b, the contribution of the twin boundary energy to the total energy was calculated using the experimentally measured twin spacing. This twin spacing arises from a balance between the total twin boundary energy and transformation strain energy. Here we use a simple energy argument to

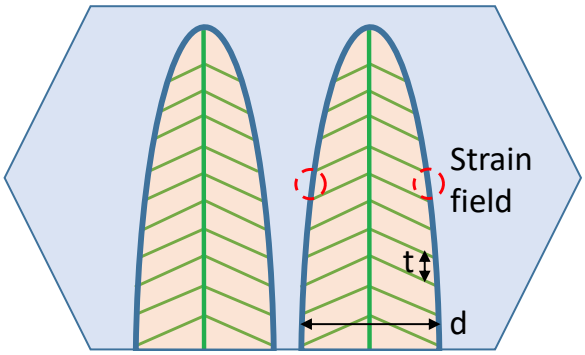

Figure 9. Schematic of martensite growth mode. The yellow regions are large martensite twin plates. The blue region is austenite; the green lines are twin planes. The red circles represent the cylindrical volumes that is affected by the M-A interfacial strain in individual small twin plates.

derive an estimate of the twin spacing and the magnitude of the strain energy from *ab initio* parameters. Suppose that martensitic growth occurs as shown schematically in Figure 9. Because twinning localizes the compatibility strain field to the M-A interface, we assume the strain energy is uniformly distributed in the cylindrical volumes marked by the red circles in Figure 9. For a single twin plate, we take the strain energy per unit depth equal to

$$E_{Strain} = 2 * \frac{1}{2} Y(1-\lambda_2)^2 * \frac{\pi t^2}{4}, \tag{1}$$

where Y is the elastic modulus of CuZr (75 GPa [21]), t is the twin width, and λ_2 is the second eigenvalue of the transformation matrix. Equation (1) assumes linear elasticity and ignores any stress relaxation as a result of defect formation. The twin boundary energy for a single twin plate is then approximately

$$E_{TB} = \gamma\, d\,, \tag{2}$$

where γ is the twin energy per unit area, and d is the width of the martensite plates. The total energy per unit volume of martensite is then given by

$$E_{Total} = \frac{1}{t\,d}(E_{Strain} + E_{TB}) = \frac{\pi t}{4d} Y(1-\lambda_2)^2 + \frac{\gamma}{t}. \tag{3}$$

The energy associated with the compatibility strain and twin boundaries is minimized when the twin spacing is given by

$$t = \frac{2}{1-\lambda}\sqrt{\frac{\gamma\, d}{\pi\, Y}}. \tag{4}$$

Taking $\lambda = 0.93$, $\gamma = 0.5\ \mathrm{J/m^2}$, and $d = 30$ nm from the results above yields a twin spacing of approximately 7.2 nm. This is on the same order of magnitude of the actual twin spacing (3.7 nm), albeit somewhat larger. We attribute this to the fact that Equation (1) does not account for the entire compatibility strain field. If the actual strain energy is larger, a finer twin structure is needed

to reduce it. Figure 10 shows the energy difference between martensite and austenite, taking into account both the compatibility strain energy and twin boundary energy as calculated from the *ab initio* simulations. It is clear that these extra energy terms have a significant impact on both the magnitude of the energy difference and its dependence on composition. Based on these results, we suggest that DFT simulations are a useful tool in guiding the experimental development of shape memory alloys, provided the energy terms associated with the fine twin structure are taken into account.

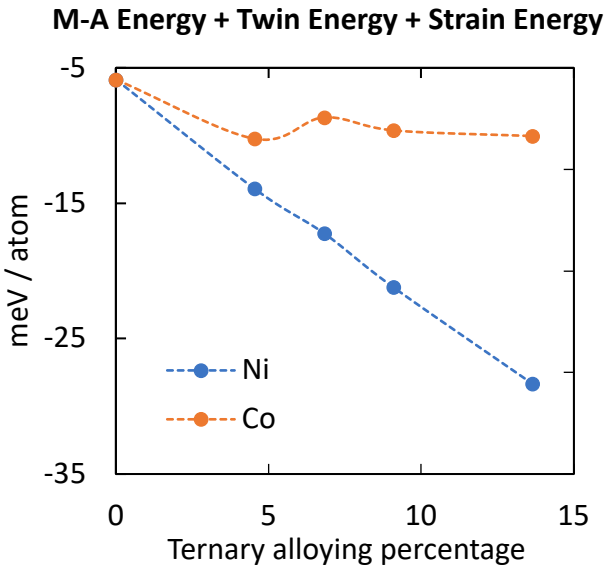

Figure 10. Adding M-A energy gap, twin boundary energy, and strain energy. Both Ni- and Co-alloys shift towards the positive side.

1.9 Undercooled Martensitic Transformation

Different types of martensitic transformation behaviors have been observed in the Cu-Zr-X system depending on the thermal history of the samples. Figure 11a shows the calorimetric signal for a $Zr_{50}Cu_{40}Ni_{10}$ sample demonstrating the various types. The first type is a gradual transformation from austenite to martensite as the temperature of the sample is lowered. This is the usual athermal behavior for martensitic transformations observed in shape memory alloys [7]. The second type, which we refer to as an explosive transformation, is an abrupt transformation where the entire sample transforms in a matter of microseconds, even though the temperature distribution in the sample is not entirely uniform. The explosive transformation occurs at significant undercooling (~60K) and results in recalescence due to the latent heat of transformation. We attribute the explosive transformation to a lack of nucleation sites for the martensite. Evidently, the number of good nucleation sites in these samples is sufficiently low that the stress wave associated with the

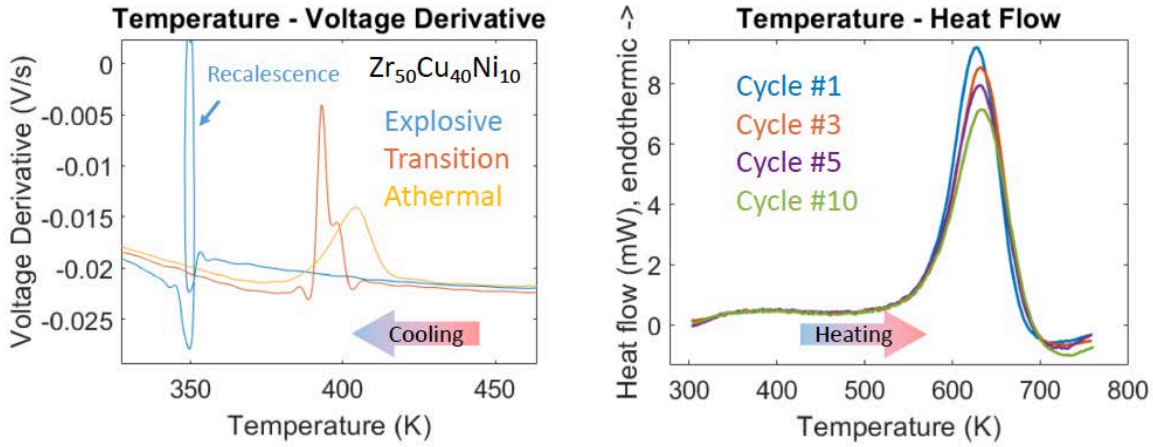

Figure 11. (a) Different martensitic transformation behaviors on cooling in the same sample. Y-axis is voltage derivative, which is a general representation of heat being released. The abrupt transformation occurs after a high-temperature scan to 1000 K. The athermal transformation occurs after a low-temperature scan to temperature right above A_f. The transitional transformation occurs after three consecutive scans to 800 K. (b) Calorimetric scan of austenite formation in the same sample on heating. Over a span of ten scans that each reach 800 K, the peak decreases in size and shifts slightly to higher temperature.

first nucleation event is sufficient to trigger nucleation elsewhere in the sample. We are unaware of any prior observation of this phenomenon.

The type of transformation observed in a given sample depends on the thermal history of the sample. If the sample is thermally cycled to right above the austenite finish temperature, the martensite transformation is of the first type, i.e., athermal. If the sample is cycled to higher temperature – approximately 1000K in the case of $Zr_{50}Cu_{40}Ni_{10}$ – the transformation is explosive. For intermediate temperatures, a transition type transformation is observed that is a combination of both types. We believe that this behavior is caused by defects that accumulate in the sample as a result of the transformation. These defects act as nucleation sites for martensite and result in athermal transformation behavior. If the sample is cycled to higher temperatures, however, the defects are annihilated and the transformation becomes nucleation limited, i.e. of the explosive type. Similarly, if the sample is annealed for one second at 800 K the transformation becomes explosive.

The transformation type seems to have a direct bearing on the functional stability of these alloys. If the alloys are thermally cycled to a temperature just above the austenite finish temperature, an athermal transformation is observed on cooling, the amount of martensite transforming to austenite on reheating decreases, and the austenite finish temperature shifts (Figure 11b). If the alloys are thermally cycled to a temperature so that an explosive transformation is observed on cooling, the amount of martensite transforming to austenite on reheating is stable and there is no temperature shift. Apparently, the defects that mediate nucleation are also responsible for shifts in functional behavior on thermal cycling.

2. Temperature-resistance sensor arrays for combinatorial study of phase transitions

The resistivity of a material is quite sensitive to the microstructure of a material and resistivity measurements have therefore been widely used in the study of bulk shape memory alloys. In the previous reporting period, we developed a very simple sensor for measuring the resistance of a thin-film sample as a function of temperature. Figure 12 shows the design of that sensor and the measurement stage. The sensor itself is made of the material of interest (e.g. CuZr or NiTi). Because of the large thermal mass of the fused silica substrate, any sample at a fixed power input will have the same temperature, regardless of the thickness or conductivity of the sample. This method allows mapping of the resistance as a function of temperature without the need for a more expensive temperature gauge.

In the current reporting period, we improved upon the previous design. The new resistivity sensor array (HP sensors) and its temperature uniformity are shown in Figure 13. HP sensors have many of the advantages of the previous design without the limitations. In particular, the sensor can be used to measure the temperature-resistance behavior of materials with low electrical conductivity

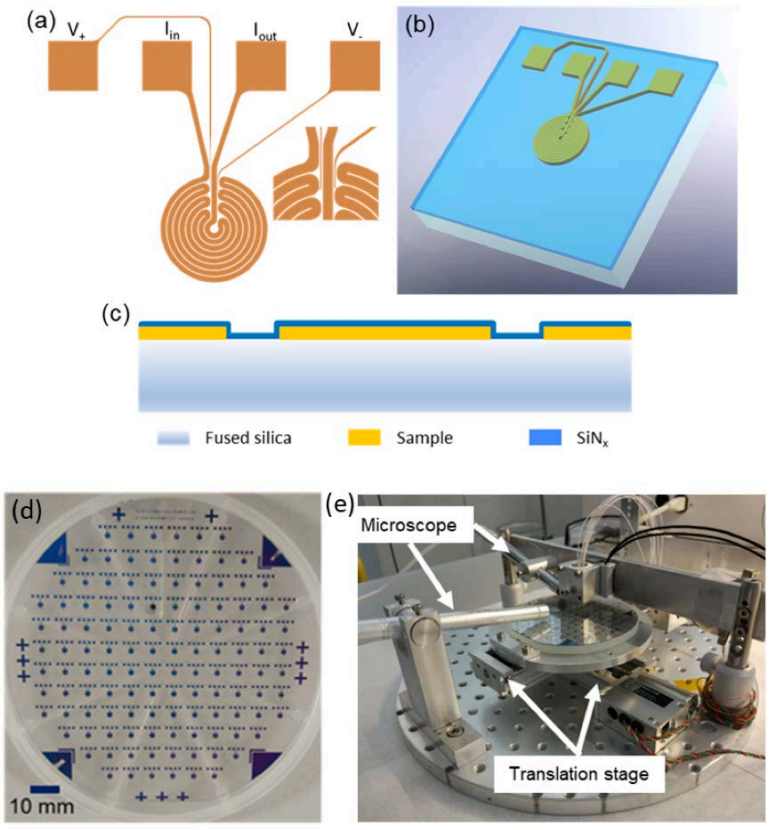

Figure 12. Resistance sensor and the measurement stage. (a) Design of the sensor. The inset shows a magnified view of the area where the voltage probes are connected to the heating element; (b) Schematic illustration of the structure of one sensor; (c) Schematic cross-section view of the sensor; (d) Optical image of an array that consists of 120 identical sensors on a 4-inch fused silica wafer. (e) Photograph of the experimental setup.

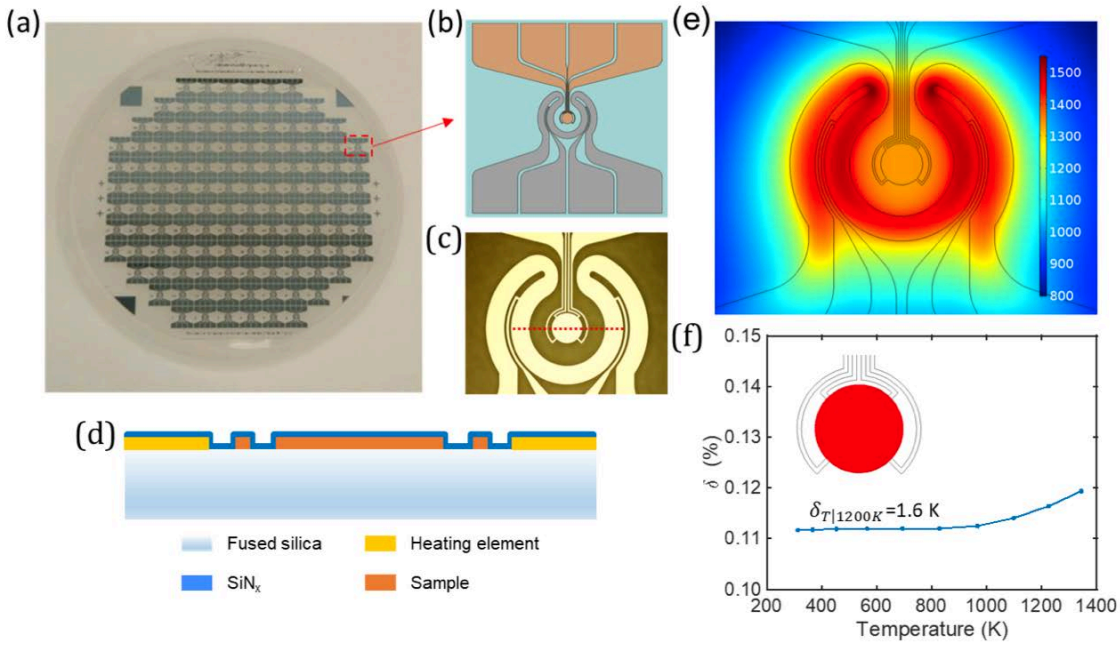

Figure 13. New HP sensor and its temperature distribution from finite element simulations (a) Optical image of 120 identical HP sensors on a fused quartz substrate; (b) Schematic diagram of the sensor design; (c) Magnified view of the sample and heating element area; (d) Schematic cross-section through part of the HP sensor along the dashed line in (c); (e) Steady-state temperature distribution obtained from a finite element simulation for an applied voltage of 10 V; temperature scale is in Kelvin; (f) Temperature non-uniformity of the sample (red region in inset) as a function of temperature as determined from finite element simulations.

such as semiconductors. This is achieved without adding much complexity to the fabrication process by using a separate resistor to heat the sample. Furthermore, the use of a separate heating element allows control of the sample temperature through use of a fixed heating voltage profile without feedback control. Finite element simulations show the excellent temperature uniformity in the sample, which is critical for the detection of subtle phase transitions.

We have demonstrated the capability of the sensor to detect a broad range of phase transformations in two types of materials systems, i.e., shape memory alloys and metallic glasses. Figure 14a shows the temperature-resistance curve of an as-deposited $Ti_{51}Ni_{43}Cu_6$ sample that was heated to approximately 850 K at a rate of 28 K/min and then cooled to room temperature. The resistance in the figure is normalized by the initial resistance at ambient temperature. The resistance decreases with increasing temperature and then drops abruptly at 680 K. At approximately 750 K, the resistance starts to rise again. The abrupt drop in resistance is associated with the onset of crystallization of the samples. Prior to crystallization the resistance decreases with increasing temperature, while after crystallization it increases. Crystalline alloys typically exhibit a positive temperature resistance coefficient as a result of increased phonon scattering. Amorphous alloys, on the other hand, can have negative or positive temperature resistance coefficients with mixed

behavior observed sometimes even in the same alloy [22]. Clearly, the behavior on heating observed in Figure 14a is typical for an amorphous sample. On cooling, the resistance decreases as expected for a crystalline material. At 320 K, however, the resistance starts to increase again. Figure 14b shows a subsequent scan that illustrates the low-temperature behavior in more detail. This behavior is typical for a thermoelastic martensitic transformation [23]. On cooling, austenite starts to transform to martensite at approximately 320 K as defined by the tangent method, while on heating the reverse transformation starts at 302 K. The transformation has a hysteresis of approximately 10 K. These observations are consistent with results reported for a similar thin-film sample of $Ti_{51}Ni_{43}Cu_6$ on a SiO_2-coated substrate [24]. The HP sensors are currently being used to investigate the Cu-Zr-X compositional space.

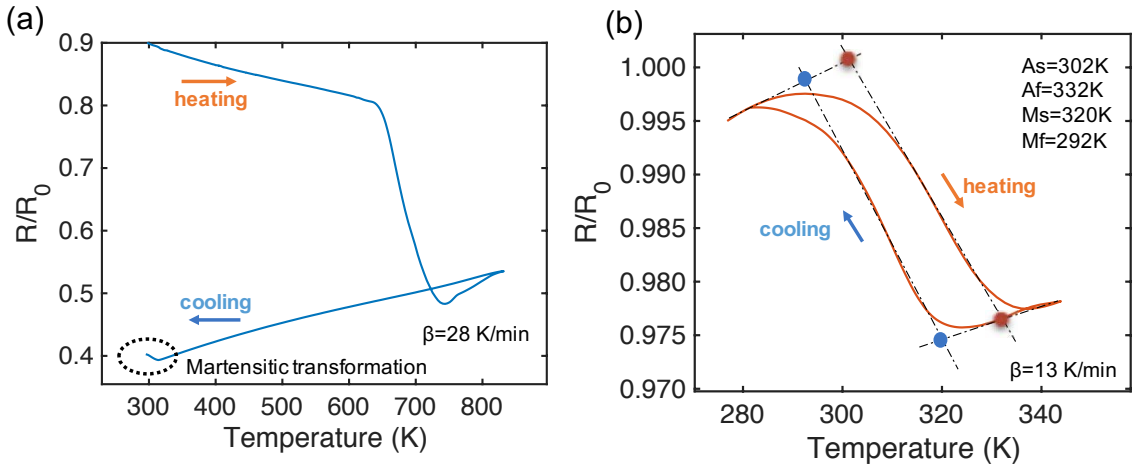

Figure 14. Temperature-resistance curves for two successive scans on $Ti_{51}Ni_{43}Cu_6$; (a) First scan on an as-deposited sample at a heating rate of 28 K/min; (b) Second scan at a heating rate of 13 K/min on the same sample showing a reversible martensitic transformation.

3. Binary Alloy Database

In displacive transformations, the symmetry relationships between parent and daughter phases establishes boundary constraints on the nodes of a PES (Potential Energy Surface). The transformations from node to node are defined by the stretch matrix, orientation relationship, and atomic correspondence. There are many possible pathways between any number of nodes, but the most probable pathways are the MEPs (Minimum Energy Pathways). Last reporting period we employed DFT calculations to find the stable polymorphs of pure CuZr, which were then used to trace possible lines of symmetry reduction. We analyzed the lattice instabilities and group-subgroup hierarchy of CuZr in order to help explain the experimentally observed preference of Cm formation over B19'. Concurrently, we set out to build a high-throughput PES (Potential

Energy Surface) sampling framework for the exploration and database generation of binary intermetallic alloys that will be used to build predictive models.

In the current reporting period, the database now contains the 4D PES of 100 binary alloys. Figures 15a and b show a comparison of the space group node stabilities for a subset of the binary alloys post-processed from the database. We can generate the MEPs along any nodes as shown in Figure 16. The minimum energy paths (MEPs) along the PES show distinct barrier difference at 6.25% atomic percent. These energy metrics can used as features to predict trends in transformation temperatures, hysteresis, functional stability, and increased macroscopic mechanical compatibility between martensite variants. The database sampling modules are to be included in the efficient experimental design framework and will help extend the database by either increasing PES resolution or adding new systems.

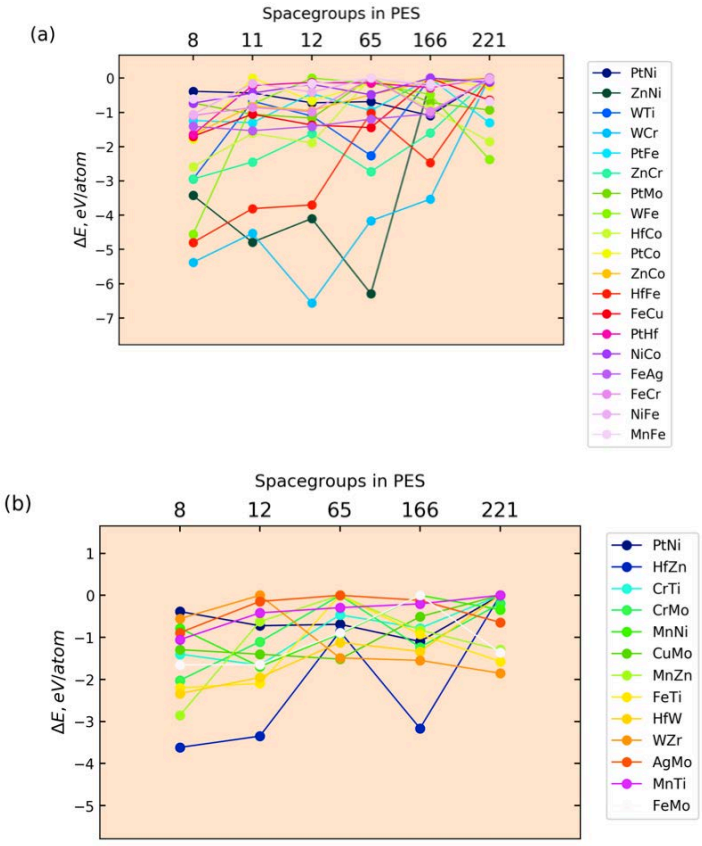

Figure 15. (a) and (b) Structures found within the 4 dimensional energy landscapes of each system. These plots were generated from the database of binary alloys. This PES model assumes that the displacive transformation can be characterized by a distinct separation between short range atomic shuffles and the lattice degrees of freedom, which include lattice strain, angular shear, and volume change. The PES was constituted from 60 calculated points sampled from a 9x9x9x9 (4 degrees of freedom) parameter space using the hyper Latin cube sampling method.

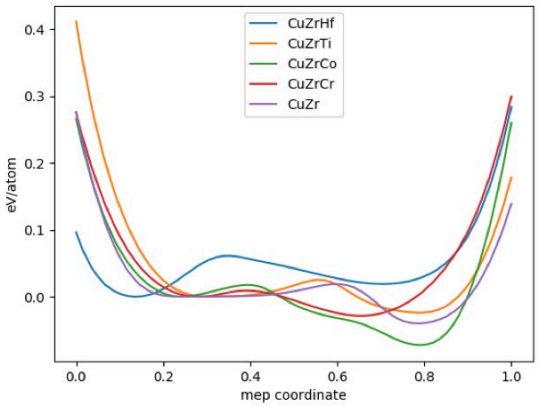

Figure 16. Minimum energy paths along 4 dimensional PES for CuZrX with alloying concentration of 6.25%.

4. Efficient Experiment Design

In this reporting period, we showed a proof of concept framework that incorporates various ideas from Data Science, Machine Learning, Artificial Intelligence and Optimal Experimental Design. These included several key elements for the completion of the overarching goal – The autonomous discovery of novel HTSMAs. The framework demonstrated an efficient exploration of the MAX ternary carbide/nitride space through Density Functional Theory (DFT) calculations. The problem was formulated with the goal of identifying the material/materials with i) the maximum bulk modulus K and ii) the maximum bulk modulus and minimum shear modulus. The case of the maximum bulk modulus K was designed as a single-objective optimization problem while the second problem was designed as a multi-objective problem. Features describing the relation between the material and objective functions were culled from literature and domain knowledge. Feature correlations were used to finalize six different feature sets which are denoted as F1, F2, F3, F4, F5 and F6. Complete details may be found at: https://arxiv.org/abs/1803.05460. As shown in Figure 17, the techniques implemented reached convergence even with smaller datasets (N=5). This is advantageous, since in real-world problems, scarcity of data is a common limitation.

We also showcased how Bayesian Model Averaging (BMA) could be leveraged in autonomous systems to direct feature selection. Figure 18(a) shows the swarm plots indicating the number of calculations required to discover the maximum bulk modulus in the MDS for for N =10 using first- and second-order BMA, respectively. The runs were cutoff of 100 calculations, so the data at ordinate 100 indicates instances that failed to converge. It can be seen that for a very high percentage of cases the maximum bulk modulus can be found within the designated budget. The width of the swarm plot tells us how quickly convergence was reached over all the instances. Plots wider at the bottom (F1,BMA_1, BMA_2) indicate that a larger fraction of the instances converged within 40 calculations. The swarm plot for F2 shows a rather large number of instances at 100, indicating that most instances failed to converge. In Figure 18(b), the average model coefficients

(posterior model probabilities) of the models based on different feature sets over all instances of initial data set are shown with the increasing number of calculations for BMA_1. Thus we see that, while prior knowledge about the fundamental features linking the material to the desired material property is certainly essential to build the Materials Design Space (MDS), the BMA approach may be used to auto-select the best features/feature sets in the MDS, thereby eliminating the requirement of knowing the best feature set a priori. Also, this framework is not significantly dependent on the size of the initial data, which enables its use in materials discovery problems where initial data is scant.

In the future, we will leverage our findings on the Cu-Zr-X system in an autonomous discovery framework. Due to the significant effect of twinning energy on the relative phase stabilities, we plan to optimally develop models that reduce computational cost of twin calculations. These models will help guide subsequent experimental sample points by detecting regions in composition space with increased probability of meeting the desired material criteria. Our efforts will focus on beginning a self-driven loop of materials discovery that minimizes unnecessary human intervention by autonomously fusing theory and experiment. A schematic depicting our advancing direction is seen in Figure 19.

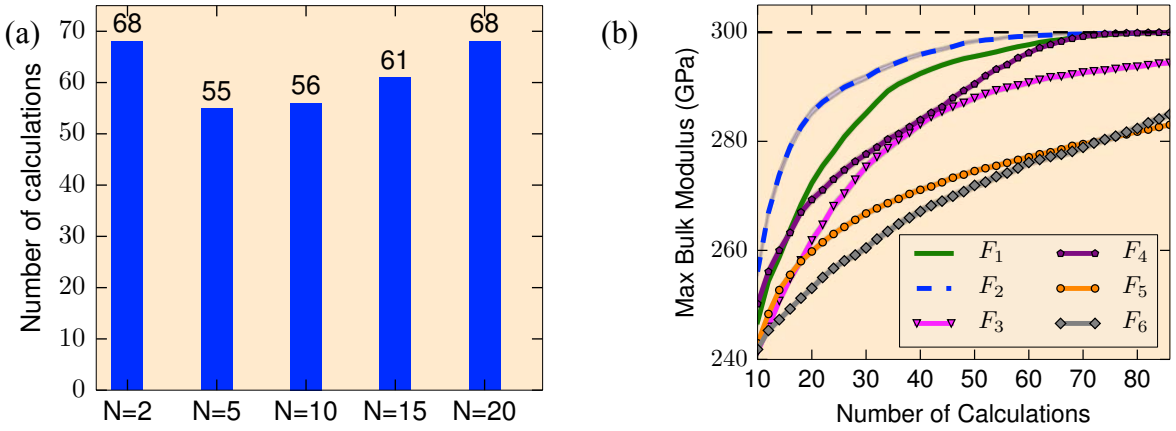

Figure 17 (a) Average number of calculations required to find maximum bulk modulus for different numbers of initial data instances N = 2, 5, 10, 15, 20 and b) Representative results for single objective optimization (maximization of bulk modulus) for N=10: Average maximum bulk modulus discovered using all described feature sets.

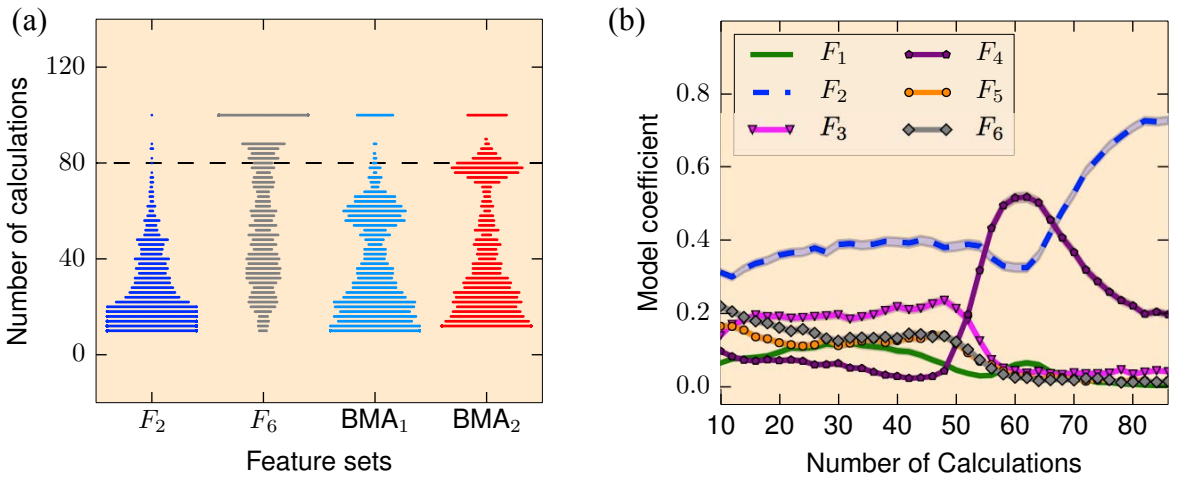

Figure 18 (a) swarm plots indicating the distribution of the number of calculations required for convergence using best feature set F_2, worst feature set F_6, BMA_1 and BMA_2. (b) average model probabilities for maximizing bulk modulus using BMA_1.

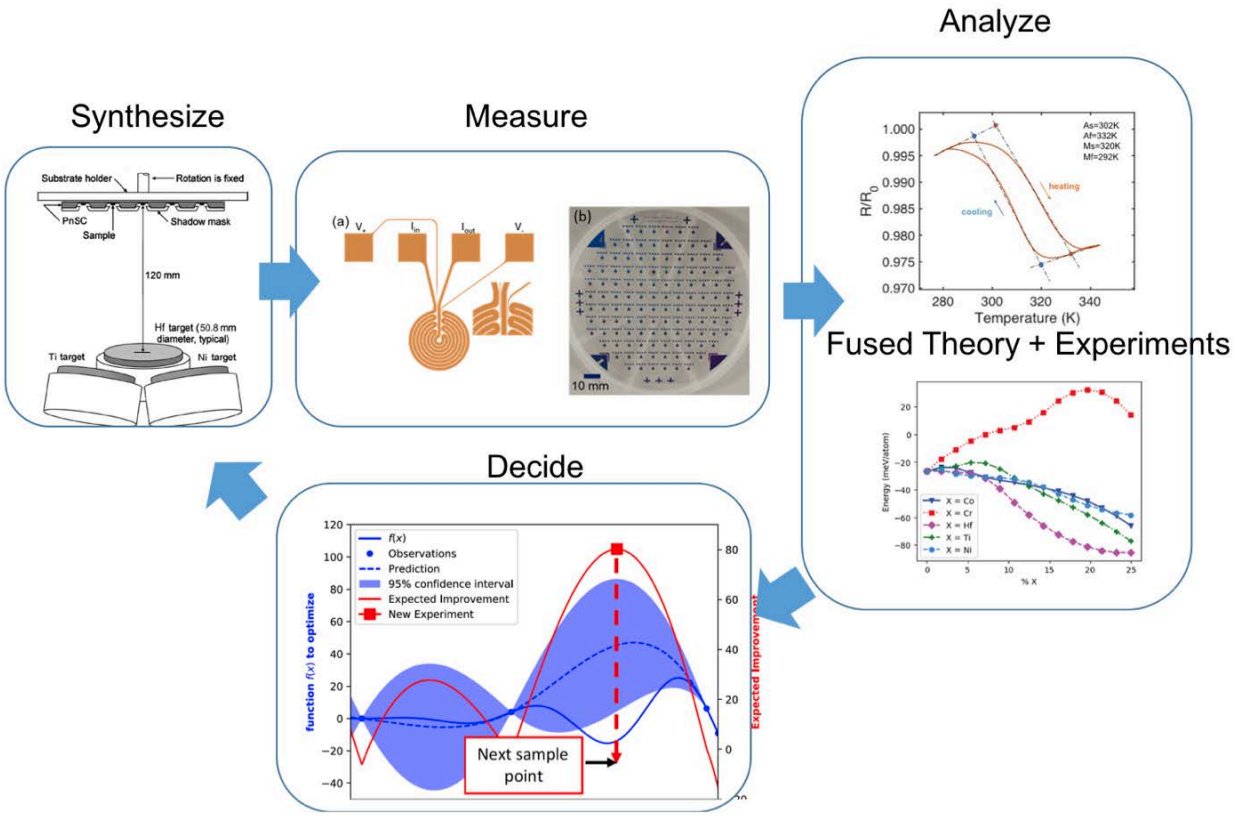

Figure 19 A schematic outlining our envisioned approach in a Bayesian Optimization based Materials Discovery Framework.

Summary

We have carried out a detailed investigation of the Cu-Zr-X (X=Ni/Co/Hf) shape memory alloy system using both experimental and computational methods. The contributions of twin boundary energy and martensite-austenite strain energy are estimated by *ab initio* simulations. Our results indicate that Cu-Zr-Ni is a promising HTSMA candidate that merits further exploration. Our database and experimental-computational framework provide useful insights into the development of novel SMAs. Results from the past year includes:

- Experiments show that the kinetics of the eutectoid reaction that forms the austenitic phase is faster in Cu-Zr-Ni alloy than in both the binary CuZr and the Co- or Hf-containing ternary alloys.
- Alloying CuZr with either Ni or Co reduces the hysteresis of the martensitic transformation, while Hf increases hysteresis. These observations are in agreement with the value of the middle eigenvalue of the martensitic transformation matrix, which is calculated from the *ab initio* lattice parameters.
- Simulations of pristine martensite and austenite suggest that both Ni and Co should increase the transformation temperature of CuZr, while Hf has little effect. Experimentally, it is observed that adding Co reduces the martensitic transformation temperature. We attribute this to the fact that martensite does not grow in austenite as a pristine phase, but is heavily twinned as a result of the compatibility strains at the martensite-austenite interface. Adding the energy terms representing the twin boundaries and the compatibility strain has a significant impact on both the magnitude of the energy difference between the two phases and its dependence on composition. Based on these results, we suggest that DFT simulations are a useful tool in guiding the experimental development of shape memory alloys, provided the appropriate energy terms are taken into account.
- We have developed new sensor arrays to measure the electrical resistance of thin-film materials as a function of temperature and composition. We demonstrated the sensitivity and accuracy of the technique by analyzing the phase evolution in Ti-Ni-Cu shape memory alloys and PdSi-based metallic glasses.
- Modeling the twin boundaries through DFT allows a closer agreement between experiment and theory. The twinning energy was modeled as a function of composition. Since the calculation of low-symmetry twin boundaries is expensive, the incorporation of predictive models is identified as a crucial element of computational-cost reduction.
- We have generated a database of 100 binary alloys that will be used to explore promising regions in composition space that meet desired HTSMA criteria. Conjointly, this serves as a benchmark for high-throughput database generation that implements sparse sampling and

advanced interpolation schemes to reduce the computation cost. This database will be extended and improved as the need arises based on a Bayesian Optimal framework.

- This work augments earlier efforts by putting forward a framework that efficiently explores the materials design space not only accounting for resource constraints but also incorporating the notion of model uncertainty. The resulting approach combines Bayesian Model Averaging within Bayesian Optimization in order to realize a system capable of autonomously and adaptively learning not only the most promising regions in the materials space but also the models that most efficiently guide such exploration.

Publications resulting from project

1. Effect of A mixing on elastic modulus, cleavage stress, and shear stress in the Ti (Si_x Al_{1-x}) C 2 MAX phase. Son W, Gao H, Duong T, Talapatra A, Radovic M, and Arróyave R. *Physical Review B*, 2017
2. Real-time atomistic observation of structural phase transformations in individual hafnia nanorods. Hudak BM, Depner SW, Waetzig GR, Talapatra A, Arróyave R, Banerjee S, and Guiton BS. *Nature Communications*, 2017
3. Modulating the Hysteresis of an Electronic Transition: Launching Alternative Transformation Pathways in the Metal–Insulator Transition of Vanadium(IV) Oxide. Braham, Erick J., Diane Sellers, Emily Emmons, Ruben Villarreal, Hasti Asayesh-Ardakani, Nathan A. Fleer, Katie E. Farley. *Chemistry of Materials*, 2018
4. Autonomous efficient experiment design for materials discovery with Bayesian model averaging. Talapatra A, Boluki S, Duong T, Qian X, Dougherty E, and Arróyave R. *Physical Review Materials*, 2018
5. Minimal Effect of Stacking Number on Intrinsic Cleavage and Shear Behavior of $Ti_{n+1}AlC_n$ and $Ta_{n+1}AlC_n$ MAX Phases. Son, Woongrak, Thien Duong, Anjana Talapatra, Evan Prehn, Zeyi Tan, Miladin Radovic, and Raymundo Arróyave. *Journal of Applied Physics*, 2018
6. Experiment Design Frameworks for Accelerated Discovery of Targeted Materials Across Scales. Talapatra, Anjana, Shahin Boluki, Pejman Honarmandi, Alexandros Solomou, Guang Zhao, Seyede Fatemeh Ghoreishi, Abhilash Molkeri. *Frontiers in Materials*, 2019
7. Phase transformations in equiatomic CuZr shape memory thin films analyzed by differential nanocalorimetry. Zheng J, Miao Y, Zhang H, Chen S, Lee D, Arróyave R, and Vlassak JJ. *Acta Materialia*, 2018
8. Combinatorial temperature resistance sensors for the analysis of phase transformations demonstrated for metallic glasses. Zhang H, Lee D, Shen Y, Miao Y, Bae J, Liu Y, Schroers J, Xiang Y, and Vlassak JJ. *Acta Materialia*, 2018
9. On the Fast Kinetics of B2–L21 Ordering in Ni-Co-Mn-In Metamagnetic Shape Memory Alloys. Wang, Yuhao, Daniel Salas, Thien C. Duong, Bharat Medasani, Anjana Talapatra, Yang Ren, Yuriy I. Chumlyakov, Ibrahim Karaman, and Raymundo Arróyave. *Journal of Alloys and Compounds*, 2019
10. Diffusion kinetics in binary CuZr and NiZr alloys in the super-cooled liquid and glass states studied by nanocalorimetry. Lee D, and Vlassak JJ. *Scripta Materialia*, 2019
11. Temperature-resistance sensor arrays for combinatorial study of phase transitions in shape memory alloys and metallic glasses. Zheng J, Zhang H, Miao Y, Chen S, and Vlassak JJ. *Scripta Materialia*, 2019
12. Dynamically Evolving Metastability in an Atomic Hourglass: Temporal Control of the Metal-Insulator Transition of VO2 by a Mobile Dopant. Diane G. Sellers, Erick J. Braham, Ruben Villarreal, Timothy D. Brown, Theodore E.G. Alivio, Heidi Clarke, Luis R. De Jesus, Lucia Zuin, Raymundo Arroyave, Patrick J. Shamberger, Sarbajit Banerjee. Submitted to *Nature*

13. Nanocalorimetry and ab initio study of ternary elements in CuZr-based shape memory alloy. Miao Y, Villarreal R, Talapatra A, Arróyave R, and Vlassak JJ. Submitted to *Acta Materialia*
14. Exploration of Phase Transformation Paths in NiTi. Talapatra, Anjana, and R Arroyave. Under preparation.
15. Nanocalorimetry study of defects in ZrCuNi thin-film shape memory alloy. Miao Y, Villarreal R, Arróyave R, and Vlassak JJ. Under preparation

References

[1] J. Zheng, Y. Miao, H. Zhang, S. Chen, D. Lee, R. Arróyave, J.J. Vlassak, Phase transformations in equiatomic CuZr shape memory thin films analyzed by differential nanocalorimetry, Acta Mater. 159 (2018) 320–331. doi:10.1016/j.actamat.2018.08.015.

[2] D. Lee, B. Zhao, E. Perim, H. Zhang, P. Gong, Y. Gao, Y. Liu, C. Toher, S. Curtarolo, J. Schroers, J.J. Vlassak, Crystallization behavior upon heating and cooling in Cu50Zr50 metallic glass thin films, Acta Materalia 121 (2016) 68–77. doi:10.1016/J.ACTAMAT.2016.08.076.

[3] P. Nash, C.S. Jayanth, The Ni−Zr (Nickel-Zirconium) system, Bull. Alloy Phase Diagrams. 5 (1984) 144–148. doi:10.1007/BF02868950.

[4] X.J. Liu, H.H. Zhang, C.P. Wang, K. Ishida, Experimental determination and thermodynamic assessment of the phase diagram in the Co–Zr system, J. Alloys Compd. 482 (2009) 99–105. doi:10.1016/J.JALLCOM.2009.04.032.

[5] P.R. Subramanian, D.E. Laughlin, The Cu-Hf (copper-hafnium) system, Bull. Alloy Phase Diagrams. 9 (1988) 51–56. doi:10.1007/BF02877460.

[6] E. Perim, D. Lee, Y. Liu, C. Toher, P. Gong, Y. Li, W.N. Simmons, O. Levy, J.J. Vlassak, J. Schroers, S. Curtarolo, Spectral descriptors for bulk metallic glasses based on the thermodynamics of competing crystalline phases., Nat. Commun. 7 (2016) 12315. doi:10.1038/ncomms12315.

[7] J.C. Fisher, J.H. Hollomon, D. Turnbull, Nucleation, J. Appl. Phys. 19 (1948) 775–784. doi:10.1063/1.1698202.

[8] G.S. Firstov, J. Van Humbeeck, Y.N. Koval, Peculiarities of the martensitic transformation in ZrCu intermetallic compound - potential high temperature SMA, Le J. Phys. IV. 11 (2001) Pr8-481-Pr8-486. doi:10.1051/jp4:2001880.

[9] C.A. Biffi, A. Figini, A. Tuissi, Influence of compositional ratio on microstructure and martensitic transformation of CuZr shape memory alloys, Intermetallics. 46 (2014) 4–11. doi:10.1016/J.INTERMET.2013.10.018.

[10] F. Meng, K. Tsuchiya, S. Ii, Y. Yokoyama, Influence of Ni on stability of martensitic transformation in Zr 50Cu50-xNix, J. Alloys Compd. 577 (2013) 136–140. doi:10.1016/j.jallcom.2012.01.089.

[11] T. Kosorukova, G. Firstov, Y. Koval, P. Verhovlyuk, J. Van Humbeeck, H. Noel, Structural phase transformations and shape memory effect in ZrCu along with Ni and Hf additions, MATEC Web Conf. 33 (2015) 06005. doi:10.1051/matecconf/20153306005.

[12] W.-S. Ko, S.B. Maisel, B. Grabowski, J.B. Jeon, J. Neugebauer, Atomic scale processes of phase transformations in nanocrystalline NiTi shape-memory alloys, Acta Mater. 123 (2017) 90–101. doi:10.1016/J.ACTAMAT.2016.10.019.

[13] J.W. Seo, D. Schryvers, Tem investigation of the microstructure and defects of CuZr martensite. Part II: Planar defects, Acta Mater. 46 (1998) 1177–1183. doi:10.1016/S1359-6454(97)00334-0.

[14] D. Schryvers, G.S. Firstov, J.W. Seo, J. Van Humbeeck, Y.N. Koval, Unit cell determination in CuZr martensite by electron microscopy and X-ray diffraction, Scr. Mater.

36 (1997) 1119–1125. doi:10.1016/S1359-6462(97)00003-1.

[15] R.P. Reed, The plate-like martensite transformation in Fe-Ni alloys, Acta Metall. (1967). doi:10.1016/0001-6160(67)90004-1.

[16] T. Waitz, The self-accommodated morphology of martensite in nanocrystalline NiTi shape memory alloys, Acta Mater. (2005). doi:10.1016/j.actamat.2005.01.033.

[17] Y. Song, X. Chen, V. Dabade, T.W. Shield, R.D. James, Enhanced reversibility and unusual microstructure of a phase-transforming material, Nature. 502 (2013) 85–88. doi:10.1038/nature12532.

[18] R.D. James, Z. Zhang, R.D. James, Z. Zhang, A Way to Search for Multiferroic Materials with "Unlikely" Combinations of Physical Properties, in: Springer, Berlin, Heidelberg, 2005: pp. 159–175. doi:10.1007/3-540-31631-0_9.

[19] R.D. James, K.F. Hane, Martensitic transformations and shape-memory materials, Acta Mater. 48 (2000) 197–222. doi:10.1016/S1359-6454(99)00295-5.

[20] L. Sandoval, J.B. Haskins, J.W. Lawson, Stability, structure, and suppression of the martensitic transition temperature by B19′ compound twins in NiTi: ab initio and classical simulations, Acta Mater. 154 (2018) 182–189. doi:10.1016/J.ACTAMAT.2018.05.016.

[21] J. Du, B. Wen, R. Melnik, Y. Kawazoe, Phase stability, elastic and electronic properties of Cu–Zr binary system intermetallic compounds: A first-principles study, J. Alloys Compd. 588 (2014) 96–102. doi:10.1016/J.JALLCOM.2013.11.018.

[22] C.L. Chien, S.H. Liou, Temperature dependence of resistance of amorphous metal-metal solids with wide composition ranges, J. Non. Cryst. Solids. (1984). doi:10.1016/0022-3093(84)90691-4.

[23] S. Hamann, M. Ehmann, S. Thienhaus, A. Savan, A. Ludwig, Micro-hotplates for high-throughput thin film processing and in situ phase transformation characterization, Sensors Actuators, A Phys. (2008). doi:10.1016/j.sna.2008.05.007.

[24] R. Löbel, S. Thienhaus, A. Savan, A. Ludwig, Combinatorial fabrication and high-throughput characterization of a Ti-Ni-Cu shape memory thin film composition spread, Mater. Sci. Eng. A. (2008). doi:10.1016/j.msea.2007.02.168.